Curvature regulation of the ciliary beat through axonemal twist

Pablo Sartori,[1] Veikko F. Geyer,[2] Jonathon Howard,[2] and Frank Jülicher[1]

[1]*Max Planck Institute for the Physics of Complex Systems, Nöthnitzer Straße 38, 01187 Dresden, Germany*
[2]*Department of Molecular Biophysics and Biochemistry, Yale University, New Haven, Connecticut 06520, USA*

Cilia and flagella are hairlike organelles that propel cells through fluid. The active motion of the axoneme, the motile structure inside cilia and flagella, is powered by molecular motors of the axonemal dynein family. These motors generate forces and torques that slide and bend the microtubule doublets within the axoneme. To create regular waveforms, the activities of the dyneins must be coordinated. It is thought that coordination is mediated by stresses due to radial, transverse, or sliding deformations, and which build up within the moving axoneme and feed back on dynein activity. However, which particular components of the stress regulate the motors to produce the observed waveforms of the many different types of flagella remains an open question. To address this question, we describe the axoneme as a three-dimensional bundle of filaments and characterize its mechanics. We show that regulation of the motors by radial and transverse stresses can lead to a coordinated flagellar motion only in the presence of twist. We show that twist, which could arise from torque produced by the dyneins, couples curvature to transverse and radial stresses. We calculate emergent beating patterns in twisted axonemes resulting from regulation by transverse stresses. The resulting waveforms are similar to those observed in flagella of *Chlamydomonas* and sperm. Due to the twist, the waveform has nonplanar components, which result in swimming trajectories such as twisted ribbons and helices, which agree with observations.

Cilia and flagella are slender cellular organelles that contain a motile internal structure called the axoneme. The axoneme contains a regular arrangement of nine microtubule doublets in a cylindrical geometry that is associated with additional structural elements such as radial spokes, a central pair of microtubules, motor proteins in the axonemal dynein family, and other elements such as nexin linkers [1,2]; see Fig. 1(a). The axoneme undergoes regular oscillatory bending waves that propel cells through fluids, and fluids across the surfaces of cells. This beat is powered by the dyneins, which generate sliding displacements between adjacent doublets [3]. Bending of the axoneme originates from the imbalance of dynein motors on opposite sides of the bending plane [4,5]. For instance, bending of the axoneme schematized in Fig. 1(a) occurs when motors above the dashed line (beating plane) dominate over those below, or vice versa. The coordinated on and off switching of the motors on opposite sides of the axoneme results in periodic bending waves.

It has been suggested that the switching of dynein activity between opposite sides of the axoneme is the result of feedback [4,6–8]. The axonemal dyneins generate forces deforming the axoneme; the deformations or the corresponding stresses, in turn, act as a signal that regulates the dyneins. To regulate motors, this signal has to affect motors on opposite sides of the axoneme antagonistically, activating those on one side of the beating plane while at the same time deactivating those on the other. Such reciprocal antagonism leads to a tug-of-war between motors across the axoneme with a winner-take-all outcome (i.e., a switch). An example of an antagonistic signal is interdoublet sliding: when the axoneme bends, the sliding is in one direction on one side of the beating plane and in the other direction on the other side. Sliding regulation has been shown to generate beating patterns [6,7,9,10].

Doublet curvature is also antagonistic across the axoneme, and was one of the earliest proposals for beat regulation [5,11,12]. Importantly, it has recently been shown

that regulation by curvature can accurately reproduce the waveforms of isolated *Chlamydomonas* axonemes, whereas regulation by sliding forces fails to generate propagating waves [13,14]. However, there is no clear mechanism by which motors can sense curvature. The reason is that the strains resulting from curvature changes in the axoneme are very small, 0.5% or 0.2 Å per tubulin subunit (for a typical maximum curvature of radius 4 μm, [14]). Such strains would be exceedingly difficult to be sensed by the small microtubule binding domain of dynein [15,16]. Given the recent support for curvature regulation, a key question remains open: how can motors sense curvature?

Another proposal for beat regulation, referred to as the "geometric clutch," is that dynein is regulated by transverse stress, which tends to separate the doublets. However, for nontwisted waveforms, the transverse stress is not antagonistic because the rotational symmetry of the axoneme implies that bends in either direction cause the same transverse and radial stresses (a result that we will establish rigorously in this paper). Regulation by transverse stress, therefore, requires an additional asymmetry [5,17,18], whose origin remains elusive. The same problem occurs in regulation by radial stresses, which tend to increase the diameter of the axonemal cross section.

To address the question of how motors can sense curvature, a three-dimensional description of the axoneme is necessary. Only then can the issue of motor antagonism be directly addressed. Furthermore, a three-dimensional model is necessary to distinguish between radial and transverse stresses. Finally, a three-dimensional model is necessary to address the role of twist.

There are two reasons to think that twist may exist in axonemes. First, axonemal dynein is known to generate a torque that rotates microtubules in gliding assays [19,20]. The handedness of the rotation corresponds to a negative twist, as defined below. And second, cilia and flagella often have
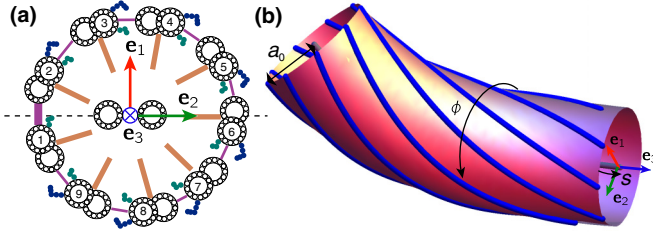
FIG. 1. Geometry of the axoneme. (a) Schematic of an axonemal cross section of radius a_0, with numbering for the nine doublets, as seen from the basal end. Dyneins appear in blue and green, elastic linkers in purple, and radial spokes in orange. The cross-bridges between doublets 1-2 (thick purple lines) define the beating plane (dashed line). The centerline triad is oriented such that $\mathbf{e}_1$, in red, points between doublets 3 and 4, and the beating plane is spanned by $\mathbf{e}_2$, in green, and $\mathbf{e}_3$, in blue. Bending in the direction of $\mathbf{e}_2$ requires the motors in filaments 2–5 to be active, while bending in the direction of $-\mathbf{e}_2$ requires activity of motors in filaments 6–9. (b) The bundle of filaments on the surface of a bent twisted cylinder is parametrized by the azimuthal coordinate ϕ and the arc-length s of the centerline.

chiral swimming paths [21,22], which suggests that their beat patterns are themselves chiral or twisted.

Despite some early computational attempts [23], no three-dimensional mechanical model of the axoneme exists in the literature. Thus, the dependence of the transverse and radial stresses on curvature and twist remains unaddressed, and the origin of curvature sensing remains unanswered. In this paper, we develop a mechanical model of the three-dimensional axonemal structure. This model, inspired by earlier work [24], is able to distinguish between transverse and radial stresses in the three-dimensional axonemal structure, and allows us to investigate their antagonism. We show that motor torques can generate twist, and that this twist is enough to break the symmetry of radial and transverse stresses. In particular, we show that twist leads to coupling of curvature to both transverse and radial forces, which leads naturally to alternative mechanisms of curvature sensing. Furthermore, the transverse stress is directly proportional to curvature, which results in beating patterns analogous to those of curvature regulation that were shown in Ref. [13] to agree with the beat of *Chlamydomonas* axonemes. Importantly, due to the presence of twist, the emerging beat patterns are nonplanar, and we show how this results in complex swimming trajectories such as twisted ribbons and helices, which are indeed observed [21,22].

I. CONTINUUM MECHANICS OF THE AXONEME

We characterize the axonemal structure by a bundle of filaments corresponding to the microtubule doublets that are arranged on the surface of a cylindrical sheet of radius a_0 [24]; see Fig. 1. Estimates of all geometric and mechanical parameters can be found in the last section of the Appendix.

The cylindrical sheet $\mathbf{R}(s,\phi)$ is parametrized by an angular coordinate ϕ and the distance variable s as

$$\mathbf{R}(s,\phi) = \mathbf{r}(s) + \mathbf{e}_1(s)a_0\cos(\phi) + \mathbf{e}_2(s)a_0\sin(\phi). \quad (1)$$

Here, s is the arc-length of the centerline $\mathbf{r}(s)$ of the cylindrical sheet measured from base to tip. The vectors $\mathbf{e}_1$ and $\mathbf{e}_2$ are unit

vectors normal to the centerline with unit tangent $\mathbf{e}_3 = \partial_s\mathbf{r}$. We choose $\mathbf{e}_1$ to point between filaments $n = 3$ and 4, and we orient $\mathbf{e}_2$ perpendicular to both $\mathbf{e}_1$ and $\mathbf{e}_3$; see Fig. 1(a). The angular parameter ϕ starts at $\mathbf{e}_1$ and grows positive clockwise toward $\mathbf{e}_2$. It is used to identify filaments, which correspond to the values $\phi = \phi_n$ with $\phi_n = 2\pi(n-4)/9 + \pi/9$.

The geometry of the filaments is fully characterized by the axonemal curvatures and twist of the centerline. The in-plane curvature is $\Omega = \mathbf{e}_3 \cdot \partial_s\mathbf{e}_2$, and the twist is $\Pi = \mathbf{e}_2 \cdot \partial_s\mathbf{e}_1$. In the following, we will focus on the case of almost planar and weakly twisted axonemal shapes. Physically this corresponds to enforcing the constraint $\mathbf{e}_3 \cdot \partial_s\mathbf{e}_1 = 0$. A more general case is discussed in the Appendix; see Eq. (A1) and below.

To discuss the mechanics of the axoneme, we introduce the relevant deformation variables. We fix the cylinder radius a_0 and the separation between neighboring filaments $2\pi a_0/9$. These constraints are enforced by the radial stress σ_a and the transverse stress σ_ϕ, respectively [see Eq. (A9) in the Appendix]. We also impose incompressibility of the filaments; see [25] for a more general treatment. Two key deformation variables of the filament bundle are the sliding displacement between filaments Δ [24–26] and the filament splay Γ, which corresponds to the out-of-plane rotation of the filaments [see Eqs. (A2) and (A4) and Fig. 4(a) in the Appendix]. To linear order in the curvature and twist, we can express the sliding displacement and the splay as

$$\Delta(s,\phi) \approx \Delta_{\mathrm{b}}(\phi) - a_0^2\Pi(s) + a_0\cos(\phi)\int_0^s \Omega(s')ds', \quad (2)$$

$$\Gamma(s) \approx -a_0\Pi(s). \quad (3)$$

Note that, to lowest order in the deformations, the splay directly corresponds to axonemal twist. Here we have introduced the basal sliding Δ_{b} [27], known to be key in shaping the beating patterns [7].

Molecular motors can induce sliding displacement and filament splay by generating active stress conjugate to these strains; see Eq. (A9) and Fig. 4(b) in the Appendix. These conjugate stresses are the motor force f_{m}, which tends to slide filaments apart, and the motor torque m_{m}, which tends to induce splay. In addition to motors, passive structural elements can also generate stresses. For instance, elements that link neighboring doublets (such as nexin links) will generate a passive sliding stress $k_{\mathrm{s}}\Delta$, where k_{s} is the sliding stiffness.

In the following, radial Fourier modes in angle ϕ will play a key role. For example, the motor force can be written as $f_{\mathrm{m}} = f_{\mathrm{m}}^{(0)} + f_{\mathrm{m}}^{(1)}\cos(\phi) + \cdots$. In this analysis, we truncate the series after the first mode for simplicity. Importantly, the mode $n = 1$ is antagonistic, as it produces forces with sign $+f_{\mathrm{m}}^{(1)}$ in the region $\phi \in [-\pi/2, \pi/2]$ above the bending plane and with sign $-f_{\mathrm{m}}^{(1)}$ in the opposing region. Higher modes can be systematically taken into account if they become relevant; see the Appendix for a treatment of the second mode. Correspondingly, we also expand the net sliding force $f = f_{\mathrm{m}} + k_{\mathrm{s}}\Delta$, and the stresses σ_ϕ and σ_a in angular Fourier modes. Since the motor torque m_{m} couples to Γ, which shows no angular dependence, the angular components of m_{m} can be integrated out from the force balance; see Eq. (A9) in the Appendix. We thus do not expand the torques in angular

modes. Upper indices in parentheses in the following always denote azimuthal Fourier modes.

II. RADIAL AND TRANSVERSE STRESS IN A TWISTED AXONEME

A bent and twisted axoneme exhibits radial stress σ_a and transverse stress σ_ϕ, which may be key in regulating the motor activity. To determine their values, we first establish a static torque balance for the twist of the axoneme. In the case in which twist relaxes quickly in time, the corresponding torque balance will be quasistatic and the static torque balance will apply. The torque balance then implies

$$a_0^4 k_s \Pi - a_0^2 \kappa_1 \partial_s^2 \Pi = a_0 m_m + a_0^2 f_m^{(0)}. \qquad (4)$$

This equation shows that the cilium is twisted by motor torques m_m and also by the zeroth harmonic of motor force $f_m^{(0)}$ (i.e., the azimuthally invariant component). The corresponding twist stiffness is provided by the doublet sliding stiffness k_s. Since twisting the cilium involves bending of the doublets, the bending stiffness of the axoneme per unit angle κ_1 couples to twist. The competition of sliding and bending of the filaments during twist is characterized by the length scale $d = \sqrt{\kappa_1/a_0^2 k_s}$, at which twist deformations decay along the axoneme in response to spatially localized motor forces or torques. Note that the axonemal bending stiffness per unit angle κ_1 is related to that of an individual filament by a geometric factor of $9/2\pi$. That is, $\kappa_1 = 9\kappa_{db}/2\pi$, with κ_{db} the doublet bending rigidity. Axonemal twist is governed by torsional stiffness. Elastic linkers between neighboring microtubule doublets provide an effective torsional stiffness $a_0^4 k_s$ of the axoneme; see Eq. (4).

The transverse and radial stresses can be calculated from force balances that constrain the radius and angle variables. The full expressions of σ_a and σ_ϕ are given in the Appendix; see Eqs. (A11) and (A12). In the simple case of almost planar deformations with small twist, we have

$$\sigma_\phi^{(1)} = M_m \Omega / a_0^2, \qquad (5)$$

$$\sigma_a^{(0)} = \frac{\Omega F^{(1)}}{2a_0}, \qquad (6)$$

$$\sigma_a^{(1)} = 2f^{(1)}\Pi + 3\kappa_1 \Omega \partial_s \Pi / a_0 + \Omega M_m, \qquad (7)$$

where we have introduced the integrated torque $M_m = -\int_s^L m_m ds'$ and the integrated net sliding force $F^{(1)} = -\int_s^L f^{(1)} ds'$, with $f^{(1)} = f_m^{(1)} + k_s \Delta^{(1)}$. Figure 2 depicts the angular profiles of radial and transverse stresses. Note that $\sigma_\phi^{(0)}$ vanishes, while the first angular mode $\sigma_\phi^{(1)}$ of the transverse stress is proportional to curvature Ω. The zeroth mode of the radial stress, in Eq. (6), is a generalization of the normal stress in two-dimensional models [17,18,28]. Importantly, the antagonistic $n = 1$ modes of the radial and transverse stresses allow for motor control. These modes are enabled by motor torques that, according to Eq. (4), can result in axonemal twist. Thus, we predict only that in twisted axonemes it is possible to have regulation by transverse and radial stresses.
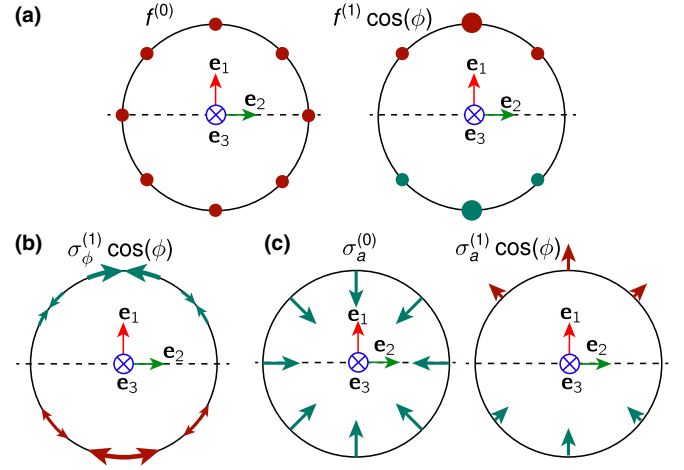
FIG. 2. Azimuthal stress profile. (a) Components of the sliding force. The zeroth mode is homogeneous and, with the motor torques, determines the twist. The first mode, positive above the dashed line (beating plane) and negative below (for $f^{(1)} > 0$), is responsible for in-plane bending. (b) and (c) The transverse stress has a first mode, and the radial stress has a zeroth and first mode. These first modes, possible only in the presence of motor torques, can regulate the first mode of the sliding force.

III. SELF-ORGANIZED BEATING BY MOTOR CONTROL FEEDBACK

We now focus our attention on self-organized beating patterns with small-amplitude waveforms and angular beat frequency ω. In this case, the periodic flagellar beat is powered by oscillating sliding forces, which we write in frequency representation as $f = \tilde{f}_0 + \tilde{f}_1 e^{i\omega t} + \cdots$, where $\tilde{f}_0$ is time-independent, $\tilde{f}_1 = \tilde{f}_{-1}^*$ is the amplitude of the fundamental Fourier mode, and higher frequency harmonics have been omitted for simplicity. We also define time Fourier modes of the azimuthal force components denoted $\tilde{f}_k^{(n)}$, as well as of the transverse stress $\tilde{\sigma}_{\phi,k}^{(n)}$, sliding $\tilde{\Delta}_k^{(n)}$, and torque $\tilde{m}_{m,k}$, where $k = -1,0,1$ and $n = 0,1,2$. These components generally depend on arc-length s.

The motor forces and torques are the result of a feedback regulation of motors by axonemal deformations [9,29]. Here we focus on the case in which the oscillating instability occurs via the oscillating force amplitude $\tilde{f}_1^{(1)}$, but not the oscillating torque amplitude $\tilde{m}_{m,1}$. We propose that motor regulation occurs through the sensitivity of the motor function to local axonemal deformations and stresses. For simplicity, we illustrate our ideas by focusing on regulation by sliding displacement [6,8,24] and by molecular deformations induced by the transversal stress [17,18,28]. We therefore write the oscillating motor force to linear order as

$$\tilde{f}_1^{(1)} = \chi(\omega)\tilde{\Delta}_1^{(1)} + \zeta(\omega)\tilde{\sigma}_{\phi,1}^{(1)}, \qquad (8)$$

where $\chi(\omega)$ and $\zeta(\omega)$ are complex frequency-dependent linear-response coefficients describing the effects of sliding displacement and transverse stress, respectively [8]. Response to the $n = 1$ mode of other stresses can in principle be added. For example, the term $\rho(\omega)\tilde{\sigma}_{a,1}^{(1)}$ would allow for response to radial stress.
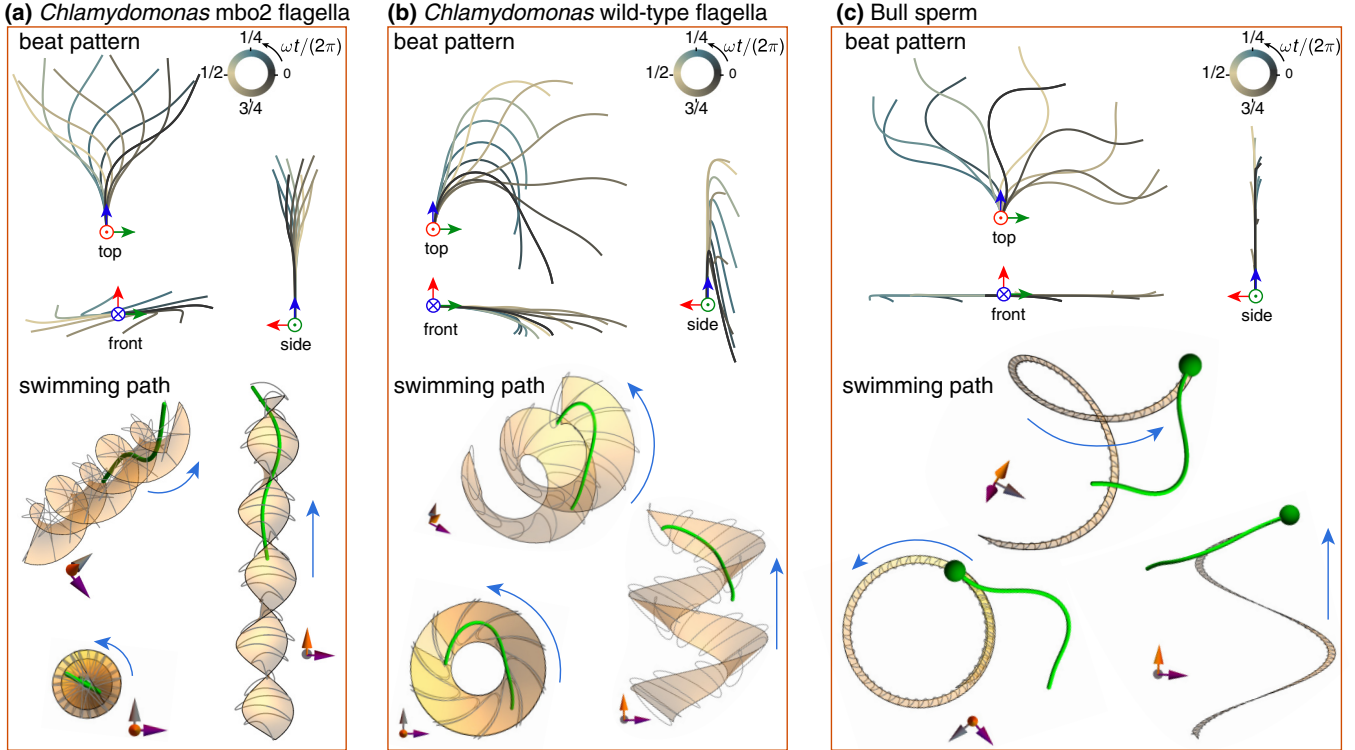
FIG. 3. Twisted beating patterns and swimming trajectories. (a)–(c) Above, top, side, and front view of self-organized beating pattern regulated by transverse stress [(a) and (b)] or sliding [(c)]. Due to the twist, all beating patterns are nonplanar, however only the waveforms in (b) and (c) are asymmetric. Below, three different views of the swimming path with a laboratory frame for reference. The gray line shows the path of the basal point, the yellow twisted surface shows the average trajectory, and the blue arrow indicates the swimming direction. For the symmetric beating pattern (a), the swimming surface forms a twisted ribbon, while for the asymmetric cases it forms a helix [(b) and (c)]. Note that due to the presence of the head, the precession of the basal end in (c) is much smaller than that in (a) and (b).

IV. SYMMETRIC AND ASYMMETRIC TWISTED BEATING PATTERNS

The dynamics of the axoneme is governed by a balance of fluid friction forces, mechanical forces of the axoneme structure, and active motor forces. These are characterized, respectively, by the friction coefficient per unit length $\xi_\perp$, the sliding and bending stiffnesses k_s and κ_1, and the motor force f_m; see Eq. (A13) in the Appendix for a general expression. This force balance gives rise to beating patterns that occur by an oscillating instability from an initially nonoscillating state. This instability can be driven by the mechanical feedbacks mediated by the regulation of motors by sliding displacements or tangential stresses described by Eq. (8). The nonoscillating state is characterized by a time-independent curvature $\Omega = \tilde{\Omega}_0$ and a time-independent twist $\Pi = \tilde{\Pi}_0$. Starting from this nonoscillating state, an oscillating mode that represents the flagellar beat can emerge. This mode can be characterized by the Fourier amplitude of the fundamental frequency component $\tilde{\Omega}_1$, which becomes nonzero beyond the instability point.

We now discuss the symmetry properties of the emerging beating patterns. We first consider the simple case of vanishing static twist $\Pi = 0$, for which beats are confined to a plane. In this case, we can distinguish symmetric beats, with vanishing average curvature $\tilde{\Omega}_0 = 0$, and asymmetric beats, with $\tilde{\Omega}_0 \neq 0$. Symmetric beats are mirror symmetric within the beat

plane [8], and the swimming trajectories are straight lines within the plane. This mirror symmetry is broken in the asymmetric case, for which swimming trajectories are circles in the plane [30].

Generally, the static twist does not vanish. The beating pattern is then confined to a twisted two-dimensional manifold; see Figs. 3(a)–3(c), bottom panels. Again, we can distinguish symmetric and asymmetric twisted beats. In the symmetric case with $\tilde{\Omega}_0 = 0$, the beat is now symmetric with respect to π rotations with a rotation axis tangential to the manifold [see Fig. 3(a)], and swimming trajectories are straight lines on the manifold. This symmetry is broken in the case of asymmetric twisted beats, which exhibit helical swimming paths [see Fig. 3(b)].

The static twist is determined from Eq. (4). The static curvature of asymmetric beats follows from the force balance $\bar{\kappa}\tilde{\Omega}_0 = \bar{a}\tilde{F}_0^{(1)}$, where $\bar{\kappa} = \pi(\kappa_1 + \kappa_2)$ is an effective bending rigidity and $\bar{a} = \pi a_0$. An approximately constant static curvature, such as that observed in *Chlamydomonas* axonemes [13,14], requires static forces that act at the distal end, in which case $F_0^{(1)}$ is s-independent. In the following, we focus on this case. For simplicity, we consider that the static torques also accumulate at the distal end, and $M_{m,0}$ is also s-independent. As a consequence, the static curvature is constant and the average shape is a twisted circular arc. We can now express the dynamic equation for the beat shape. For

the case of a symmetric twisted beat, we find

$$i\omega\xi_\perp\tilde{\Omega}_1 = -\bar{\kappa}\partial_s^4\tilde{\Omega}_1 + \pi a_0^2\chi\partial_s^2\tilde{\Omega}_1 + \pi a_0\beta\partial_s^3\tilde{\Omega}_1. \quad (9)$$

Here $\beta(\omega) = (M_{m,0}/a_0^2)\zeta(\omega)$ plays the role of an effective motor control feedback by curvature. The term proportional to χ describes a motor control feedback by sliding displacements. Regulation by transverse stress would contribute with additional geometrical terms proportional to ρ.

Equation (9) not only describes beats in a plane, but for $\Pi \neq 0$ it describes beats on a twisted two-dimensional manifold. The resulting three-dimensional shapes $\mathbf{r}(s)$ can be determined from Ω and Π, which are solutions to Eqs. (9) and (4), by integrating $\partial_s\mathbf{e}_3 = -\Omega\mathbf{e}_2$ and $\partial_s\mathbf{e}_2 = \Omega\mathbf{e}_3 - \Pi\mathbf{e}_1$. Thus, although we constrained $\mathbf{e}_3 \cdot \partial_s\mathbf{e}_1 = 0$, the twist causes out-of-plane bending. An example of such a beat is shown in Fig. 3(a) in the case in which oscillations are generated by motors that are regulated via transverse stresses. The resulting waveform is nonplanar and the swimming path corresponds to a twisted ribbon, as recently observed in sperm [31]. The planar projection of this beating pattern is analogous to that of the *Chlamydomonas* mutant *mbo2* [32], as recently shown in Ref. [13].

Asymmetric beating patterns can be studied in a similar way; see Eq. (A19) in the Appendix, which is a generalization of Eq. (9). An example of such a beating pattern for the case of motor regulation by transverse stresses is shown in Fig. 3(b). This beating pattern is nonplanar and asymmetric, and the resulting swimming path is a helical ribbon. This waveform is analogous to the one observed for the wild-type *Chlamydomonas* axoneme [33], as detailed in Ref. [13].

Alternatively, we can also discuss beats by motor regulation via sliding. It has been suggested that sliding control likely governs the beat shape of bull sperm [7]. In Fig. 3(c), we show such a beating pattern of asymmetrically beating axoneme with motors regulated via sliding. The result is a waveform similar to that of a freely swimming bull sperm. Due to the friction of the sperm head [green sphere in Fig. 3(c)], the resulting helical ribbon is narrow as compared to Fig. 3(b); see also [21,22].

V. DISCUSSION

Using a three-dimensional continuum mechanical model of the axoneme, we showed that both shear stresses (associated with sliding forces) and transverse stresses (associated with torques) can be used to regulate motors and generate periodic beating patterns. In principle, radial stresses could also regulate the motors. The key feature of all these stresses is that they are antagonistic, meaning that they have opposite sign on opposite sides of the axoneme and so will lead to switching of motor activity. Our finding is that twist, induced by motor torques, leads to coupling between curvature and transverse stress. Thus, in the presence of twist, transverse stresses are proportional to curvature. Consequently, twist provides an alternative mechanism by which the motors can sense curvature, namely through the tendency of the doublets to separate. This provides a possible solution to the problem of sensing the tiny strains associated with microtubule bending.

Dynein-generated torques induce splay deformations of microtubule doublets, which in turn lead to axonemal twist. As a consequence of the twist, beating patterns are in general

chiral. This chirality produces a nonplanar component to the waveform, which results in the swimming trajectories being either helical paths or twisted ribbons. Such swimming paths have indeed been observed experimentally for different sperm cells [21,22,31]. If such swimmers are observed near surfaces, the chirality of the beat leads to circular trajectories [34], which have been reported for many systems [30,35]. Using literature values for the mechanical properties of the axoneme together with the presented theoretical framework, the amount of expected twist was calculated as the distal twist angle, which is 0.04 rad for bull sperm and 0.25 rad for *Chlamydomonas*. These values present approximations for the expected twist sufficient to realize the proposed motor-regulation of the beat, and they can be compared to experimental studies.

Because the structure of the axoneme is three-dimensional, and the resulting beats are nonplanar (in general), we believe that our cylindrical continuum mechanical model of the axoneme will be an important tool to understand the mechanical origin of beat asymmetries and the selection of the beat plane of flagellar beats.

APPENDIX

1. Geometry of the axoneme

The axonemal structure is in general subject to radial deformations as well as deformations that alter the transverse spacing between adjacent microtubules. To account for this, we introduce the function $\varphi(s,\phi)$ describing the azimuthal angle of filaments indexed by ϕ. Similarly, we allow the cylinder radius $a(s,\phi)$ to depend on s and ϕ. Taking this into account, the geometry of the cylindrical sheet containing the filament doublets is given by

$$\begin{aligned}\mathbf{R}(s,\phi) = \mathbf{r}(s) &+ \mathbf{e}_1(s)a(s,\phi)\cos(\varphi(s,\phi))\\ &+ \mathbf{e}_2(s)a(s,\phi)\sin(\varphi(s,\phi)), \quad (A1)\end{aligned}$$

which is a generalization of Eq. (1) that allows for radial as well as transverse deformations.

To characterize the geometry of the filaments, we introduce the tangent vectors $\mathbf{e}_s = \partial_s\mathbf{R}/|\partial_s\mathbf{R}|$ and $\mathbf{e}_\phi = \partial_\phi\mathbf{R}/|\partial_\phi\mathbf{R}|$, which form a basis of the tangent space on the cylindrical sheet. We also introduce the filament normal $\mathbf{n}$ in the tangent plane. It obeys $\mathbf{e}_s \cdot \mathbf{n} = 0$ and $\mathbf{n}^2 = 1$; see Fig. 4(a). The vector $\mathbf{e}_a = \mathbf{n} \times \mathbf{e}_s$ is normal to the cylinder pointing outward. The filament curvatures tangential and perpendicular to the cylindrical surface are then given by $C_1(s,\phi) = \mathbf{e}_s \cdot \partial_s\mathbf{n}$ and $C_2(s,\phi) = \mathbf{e}_a \cdot \partial_s\mathbf{e}_s$, respectively.

We now discuss the deformation variables relevant for the mechanical description of the axoneme. For simplicity, we impose the constraints $\varphi = \phi$ and $a = a_0$ for which the cylinder radius a_0 and the separation between neighboring filaments $2\pi a_0/9$ are fixed. We also impose incompressibility of the filaments; see [25] for a more general treatment. The two most relevant deformation variables of the filament bundle
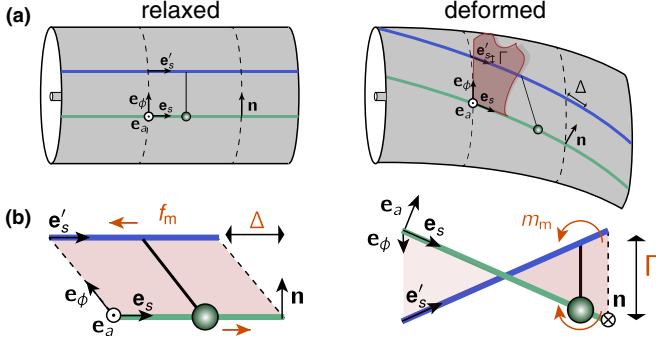
FIG. 4. Deformation of the axoneme. (a) Relaxed and deformed geometries of the axoneme with two filaments marked in green and blue, and a dynein represented as a black line with a green circle. In the deformed state, the tangent plane (in red) spanned by $\mathbf{e}_s$ and $\mathbf{e}_\phi$ does not contain the tangent vector $\mathbf{e}_s'$ of the contiguous doublet, which is displaced out of the plane by a distance Γ in the direction of $\mathbf{e}_a$. The sliding Δ corresponds to the length mismatch of the two successive doublets measured by projecting in the direction of the normal vector $\mathbf{n}$. (b) A dynein motor creates a pair of forces f_m that produces sliding Δ, and also torques m_m that produce out-of-plane displacement Γ. The deformed states are shown from different perspectives, with the tangent and normal vectors indicated.

are then the sliding displacement Δ [24–26] and the splay Γ; see Fig. 4(a). The sliding displacement is defined by

$$\Delta = a_0 \nabla_{\mathbf{n}} (\ell_b + \ell), \tag{A2}$$

where ℓ denotes the arc-length of a filament corresponding to angle ϕ at centerline distance s, with

$$\ell(s,\phi) = \int_0^s |\partial_s \mathbf{R}(s',\phi)| ds'. \tag{A3}$$

The length offset at the base, defined as the mismatch between the centerline and filament ϕ, is denoted $\ell_b(\phi)$. Correspondingly, the sliding displacement at the base is $\Delta_b = a_0 \nabla_{\mathbf{n}} \ell_b$. Here, the normal derivative is defined by $\nabla_{\mathbf{n}} f = (n^s/|\partial_s \mathbf{R}|)\partial_s f + (n^\phi/|\partial_\phi \mathbf{R}|)\partial_\phi f$, where n^s and n^ϕ are the components of $\mathbf{n} = n^s \mathbf{e}_s + n^\phi \mathbf{e}_\phi$; see [24] for details on calculating $\mathbf{n}$. The filaments splay is defined as

$$\Gamma = \mathbf{e}_a \cdot \partial_\phi \mathbf{e}_s, \tag{A4}$$

and it corresponds to the out-of-plane rotation of the filament tangent vector when changing ϕ.

The geometry of the filaments is fully characterized by the axonemal curvatures, $\Omega = \mathbf{e}_3 \cdot \partial_s \mathbf{e}_2$ and $\Theta = -\mathbf{e}_3 \cdot \partial_s \mathbf{e}_1$, the twist $\Pi = \mathbf{e}_2 \cdot \partial_s \mathbf{e}_1$, and the length offset $\ell_b(\phi)$. Thus, the curvatures of the doublets, $C_1(s,\phi)$ and $C_2(s.\phi)$, the axonemal splay Γ, and the sliding displacement Δ are functions of Ω, Θ, Π, and ℓ_b. For the case of small deformations, we have

$$C_1(s,\phi) \approx \Omega(s)\cos(\phi) + \Theta(s)\sin(\phi) - a_0\partial_s\Pi, \tag{A5}$$

$$C_2(s,\phi) \approx \Theta(s)\cos(\phi) - \Omega(s)\sin(\phi), \tag{A6}$$

where only terms linear in the axoneme curvatures are kept; see also [25]. Note that Ω and Θ correspond to curvatures in two perpendicular directions, and that in the main text we constrained $\Theta = 0$. Note also that the rate of twist, and not

the twist, affects the curvature on the tangent plane C_1. This is because, as shown in Eq. (3), a constant twist corresponds to a constant sliding. Constant twist contributes as a higher-order correction to C_2. Using these expressions and the definitions Eqs. (A2) and (A4) for sliding and splay, we arrive at

$$\Delta(s,\phi) \approx \Delta_b(\phi) - a_0^2 \Pi(s) + a_0 \cos(\phi) \int_0^s \Omega(s') ds'$$

$$+ a_0 \sin(\phi) \int_0^s \Theta(s') ds', \tag{A7}$$

$$\Gamma(s) \approx -a_0 \Pi(s). \tag{A8}$$

See [24] for details on similar calculations.

2. Work functional

The mechanical properties of the axoneme are characterized by the elasticity of filaments and linkers, and the active forces and torques generated by molecular motors. We introduce the work functional G that describes the mechanical work performed to induce axonemal deformations:

$$G = \int_0^L \int_0^{2\pi} \left\{ \frac{\kappa_1}{2} C_1^2 + \frac{\kappa_2}{2} C_2^2 + \frac{k_s}{2} \Delta^2 + \frac{k_r}{2}(\ell_b + \ell - s)^2 \right.$$

$$+ f_m \Delta + m_m \Gamma + \sigma_\phi a_0^2 (\partial_\phi \varphi - 1) + \sigma_a a_0 (a - a_0)$$

$$\left. + \frac{\Lambda}{2} |\partial_s \mathbf{r}|^2 \right\} ds\, d\phi + \int_0^{2\pi} \left\{ \frac{K_s}{2} \Delta_b^2 + \frac{K_r}{2} \ell_b^2 \right\} d\phi. \tag{A9}$$

Here κ_1 and κ_2 are bending rigidities corresponding to deformation of the filaments tangent and perpendicular to the cylindrical sheet. The sliding stiffness of elements that link neighboring doublets is denoted k_s. Similarly, k_r denotes the radial stiffness of sliding linkers between filaments and the central pair, which was ignored in the main text for simplicity. These elastic constants relate to those of an individual filament by a geometric factor of $9/2\pi$, for example $\kappa_1 = 9\kappa_{db}/2\pi$, with κ_{db} the doublet bending rigidity. The tangential stress σ_ϕ and the radial stress σ_a are Lagrange multipliers to impose the constraints $\varphi = \phi$ and $a = a_0$. The Lagrange multiplier Λ imposes the constraint $|\partial_s \mathbf{r}| = 1$. Finally, K_s and K_r are basal stiffnesses between neighboring filaments and between filaments and the central pair, respectively. The mechanical work performed by motors is given by $f_m \Delta$ and $m_m \Gamma$.

We express the ϕ dependence of variables in Eq. (A9) by Fourier series. For instance, the motor force can be written as

$$f_m = f_m^{(0)} + f_m^{(1)} \cos(\phi) + f_m^{(2)} \sin(\phi) + \cdots, \tag{A10}$$

with $f_m^{(n)}$ unknown functions of the arc-length. In the main text, we considered the $n = 0, 1$ modes. Here we also discuss the $n = 2$ mode, which is orthogonal to $n = 1$ and causes bending in the out-of-plane direction. Correspondingly, we also expand σ_ϕ, σ_a, Δ, ℓ, and ℓ_b. Note that because Γ shows no angular dependence, in Eq. (A9) any ϕ dependence of m_m can be integrated out. We thus do not expand m_m in ϕ. The same argument holds for the Lagrange multiplier Λ.

3. Radial and transverse stress

To obtain the radial stress σ_a and the transverse stress σ_ϕ, we use the force balances given by $\delta G/\delta a = 0$ and $\delta G/\delta \varphi = 0$.

The procedure is straightforward, see [8,24,28] for similar calculations, and for σ_a directly gives

$$\sigma_a = 2(f - m_m/a_0)\Pi + F[\Omega\cos(\phi) + \Theta\sin(\phi)]/a_0$$
$$+ F_r[\Omega\sin(\phi) - \Theta\cos(\phi)]/a_0 - \kappa_1\{(\partial_s\Pi)^2$$
$$- 2\partial_s\Pi[\Omega\cos(\phi) + \Theta\sin(\phi)]/a_0\}, \qquad (A11)$$

where we have introduced the radial force $F_r = -\int_s^L k_r(\ell_b + \ell - s)ds'$, set to zero in the main text. For the case $\Theta = 0$ and to linear order in Π, the zeroth and first azimuthal modes are those in Eqs. (6) and (7), where we have used the integral of Eq. (4). In the case of the transverse stress, the force balance results in

$$a_0^2\partial_\phi\sigma_\phi = \kappa_1[\Omega\cos(\phi) + \Theta\sin(\phi) - a_0\partial_s\Pi]$$
$$\times [\Theta\cos(\phi) - \Omega\sin(\phi)]$$
$$- \kappa_2[\Theta\cos(\phi) - \Omega\sin(\phi)][\Theta\sin(\phi) + \Omega\cos(\phi)]$$
$$- a_0 F[\Theta\cos(\phi) - \Omega\sin(\phi)]$$
$$- a_0 F_r[\Omega\cos(\phi) + \Theta\sin(\phi)]. \qquad (A12)$$

For the case $\Theta = 0$, we have $a_0^2\partial_\phi\sigma_\phi = (a_0 F^{(0)} + a_0\kappa_1\partial_s\Pi)\Omega\sin(\phi) + \cdots$. Using Eq. (4) and integrating gives the harmonic in Eq. (5).

4. General equations of motion

In the case in which the twist Π relaxes fast over time, the torque balance is determined by $\delta G/\delta\Pi = 0$, which results in Eq. (4); see [24] for a characterization of twist dynamics. The dynamics of the centerline $\mathbf{r}$ is governed by a balance of fluid friction forces and axonemal forces,

$$\partial_t\mathbf{r} = -(\xi_\perp^{-1}(\mathbf{e}_1\mathbf{e}_1 + \mathbf{e}_2\mathbf{e}_2) + \xi_\parallel^{-1}\mathbf{e}_3\mathbf{e}_3)\cdot\frac{\delta G}{\delta\mathbf{r}}. \qquad (A13)$$

Here $\delta G/\delta\mathbf{r}$ is the axonemal force, and $\xi_\perp$ and $\xi_\parallel$ are the friction coefficients per unit length perpendicular and tangential to the axonemal axis. From Eq. (A13) we can obtain dynamic equations for the axonemal curvatures Ω and Θ given by $\partial_t\Omega = -\mathbf{e}_2\cdot\partial_t\partial_s^2\mathbf{r}$ and $\partial_t\Theta = \mathbf{e}_1\cdot\partial_t\partial_s^2\mathbf{r}$. Note that we are neglecting fluid interactions, which can be relevant when two or more flagella are nearby [36,37]. This is justified by studies that show that these interactions are not necessary to understand the swimming of single flagellates with high precision [30,38,39].

The axonemal force is explicitly given by

$$\frac{\delta G}{\delta\mathbf{r}} = -\partial_s\{\mathbf{e}_1(-\bar{a}(F_t^{(1)}\Pi + f^{(2)}) + \bar{\kappa}\Omega\Pi + \bar{\kappa}\partial_s\Theta)$$
$$+ \mathbf{e}_2(-\bar{a}(F_t^{(2)}\Pi - f^{(1)}) + \bar{\kappa}\Theta\Pi - \bar{\kappa}\partial_s\Omega - \mathbf{e}_3\tau)\}, \qquad (A14)$$

where we have introduced the total force modes $F_t^{(1)} = F^{(1)} + F_r^{(2)}$ and $F_t^{(2)} = F^{(2)} + F_r^{(1)}$, the tension $\tau = 2\pi\Lambda - \bar{a}(F^{(1)}\Omega + F^{(2)}\Theta) - \bar{\kappa}(\Omega^2 + \Theta^2)$, the effective bending rigidity $\bar{\kappa} = \pi(\kappa_1 + \kappa_2)$, and the effective radius $\bar{a} = \pi a_0$. Taking the time derivative of the constraint $\partial_s\mathbf{r}^2 = 1$, we arrive at $\mathbf{e}_3\cdot\partial_s\partial_t\mathbf{r} = 0$, which together with Eq. (A13) provides the equation for the tension. Finally, to calculate the modes of the basal length $\ell_b^{(n)}$, we use the sliding force balances $\delta G/\delta\ell_b^{(n)} =$

0. For $n = 1$ and 2, the equations are $K_t\ell_b^{(1)} = F_t^{(2)}(0)$ and $K_t\ell_b^{(2)} = F_t^{(1)}(0)$, while doing $\delta G/\delta\ell_b^{(0)} = 0$ results in $\ell_b^{(0)} = 0$. Here, we have defined the total basal stiffness $K_t = K_s + K_r$.

The boundary forces and torques exerted by the filament correspond to the boundary terms of $\delta G/\delta\mathbf{r}$ and $\delta G/\delta\Pi$; see [8,24,28]. Balancing these by external forces $\mathbf{F}_{ext}$ and torques $\mathbf{T}_{ext}$, we have at the base $s = 0$:

$$\mathbf{F}_{ext} = -(-\bar{a}(F_t^{(1)}\Pi + f^{(2)}) + \bar{\kappa}\Omega\Pi + \bar{\kappa}\partial_s\Theta)\mathbf{e}_1$$
$$- (-\bar{a}(F_t^{(2)}\Pi - f^{(1)}) + \bar{\kappa}\Theta\Pi - \bar{\kappa}\partial_s\Omega)\mathbf{e}_2 + \tau\mathbf{e}_3, \qquad (A15)$$

$$\mathbf{T}_{ext} = (\bar{a}F^{(2)} - \bar{\kappa}\Theta - \pi\kappa_1 a_0^2\Omega\partial_s\Pi)\mathbf{e}_1$$
$$+ (-\bar{a}F^{(1)} + \bar{\kappa}\Omega + \pi\kappa_1 a_0^2\Theta\partial_s\Pi)\mathbf{e}_2, \qquad (A16)$$

$$M_{ext} = \kappa_1 a_0\partial_s\Pi. \qquad (A17)$$

The lack of a third component in the torque balance comes from neglecting the twist dynamics [24]. The third moment balance comes from the contribution of filament bending, and involves an additional external moment M_{ext}. At the tip $s = L$, the boundary conditions are analogous. In this work, we considered two types of boundary conditions. For a freely swimming flagellum, the external forces and torques are null. For a flagellum attached to a head, the torques and forces at the base are $\mathbf{F}_{ext} = \xi_{trans}\mathbf{v}$ and $\mathbf{T}_{ext} = \xi_{rot}\boldsymbol{\omega}$, where $\boldsymbol{\omega} = (e_3\cdot\partial_t e_2, e_1\cdot\partial_t e_3, e_2\cdot\partial_t e_1)_0$ and $\mathbf{v} = \partial_t\mathbf{r}_0$ are the head's rotational and translational velocities, with the subindex 0 indicating evaluation at $s = 0$, and ξ_{trans} and ξ_{rot} the corresponding friction coefficients of the head.

5. Weakly nonplanar dynamics of the axoneme

In the main text, we focus on the case of almost planar and weakly twisted axonemal shapes. Physically, this corresponds to enforcing the constraint $\Theta = 0$. The nonlinear equation of motion of Ω is then to linear order in Π given by

$$\xi_\perp\partial_t\Omega = -\bar{\kappa}\partial_s^4\Omega + \bar{a}\partial_s^3 f^{(1)} + \partial_s^2(\Omega\tau)$$
$$+ (\xi_\perp/\xi_\parallel)\partial_s\{[\Omega^2(\bar{\kappa}\partial_s\Omega - \bar{a}f^{(1)}) + \Omega\partial_s\tau]\}. \qquad (A18)$$

The dynamic shape equation (A18) for the curvature Ω is a generalization of the previously introduced shape equation for two-dimensional beats [8,11,12]. Solving Eq. (A18) provides the time dependence of the curvature Ω from which, provided the twist Π, we determine the axonemal shape by integration along the arc-length. To impose the constraint of $\Theta = 0$ in the presence of twist, the component $f^{(2)}$ of the sliding force becomes a Lagrange multiplier that corresponds to the force introduced by structural elements.

The dynamics of small-amplitude periodic beats can be characterized by an equation in frequency space. To obtain it, we linearize Eq. (A18) and then transform it into Fourier space. For the case of symmetric beats, in which $\tilde{\Omega}_0 = 0$, this leads directly to Eq. (9). For asymmetric beats, we expand Eq. (A18) around a static shape given by a constant static

curvature $\tilde{\Omega}_0 = \bar{a}\tilde{F}_0^{(1)}/\bar{\kappa}$. The dynamic mode then obeys

$$i\omega\xi_\perp\tilde{\Omega}_1 = -\bar{\kappa}\partial_s^4\tilde{\Omega}_1 + \bar{a}\partial_s^3 f_1^{(1)} + (1 + \xi_\perp/\xi_\parallel)\tilde{\Omega}_0\partial_s^2\tau_1$$

$$+ (\xi_\perp/\xi_\parallel)\tilde{\Omega}_0^2\left(\bar{\kappa}\partial_s^2\tilde{\Omega}_1 - \bar{a}\partial_s f_1^{(1)}\right), \quad \text{(A19)}$$

where τ_1 is obtained from expanding the equation for the tension.

6. Twist by tip-accumulated torques

If the source of twist is a tip-accumulated torque, we have that $m_m = M\delta(s - L)$. In the case in which $f_m^{(0)} = 0$, the solution to Eq. (4) is using the boundary conditions $\partial_s\Pi(s = 0) = 0$, and $a_0\kappa_1\partial_s\Pi(s = L) = M$ is $\Pi = (Md/\kappa_1 a_0)\sinh(s/d)/\cosh(L/d)$. Note that for $L \ll d$ the twist created changes little along the length. Conversely, for $L \gg d$ the twist quickly decays away from the tip.

7. Swimming trajectories

The force density exerted by the cilium in the fluid is $\mathbf{f}_{\text{fl}} = [\xi_\perp(\mathbf{e}_1\mathbf{e}_1 + \mathbf{e}_2\mathbf{e}_2) + \xi_\parallel\mathbf{e}_3\mathbf{e}_3] \cdot \partial_t\mathbf{r}$. Imposing that the sum of all forces and torques in the fluid must vanish, we have $\xi_{\text{trans}}\mathbf{v} + \int_0^L \mathbf{f}_{\text{fl}}ds = 0$ and $\xi_{\text{rot}}\boldsymbol{\omega} + \int_0^L \mathbf{r} \times \mathbf{f}_{\text{fl}}ds = 0$, where the terms outside the integrals come from the head's drag [30,39,40]. Given a beating pattern, we can calculate $\mathbf{f}_{\text{fl}}$ and use these equations to obtain the translational and rotational velocities at each instant during the beat.

8. Parameters used

The *Chlamydomonas* cilium is $L = 10.2$ μm long and has frequency $\omega/2\pi = 73.1$ Hz, while bull sperm has $L = 58.3$ μm and $\omega/2\pi = 19.8$ Hz [7]. For bull sperm $\tilde{\Omega}_0 = 0.010$ μm^{-1} [7], for wild-type *Chlamydomonas* we took $\tilde{\Omega}_0 = 0.25$ μm^{-1} and for *mbo2* $\tilde{\Omega}_0 = 0$ [33]. The radius we used is $a_0 = 0.2$ μm [1,2].

We now estimate $\tilde{F}_0^{(1)}$ and M, note that a density of 500 μm^{-1} dyneins with a force of 0.7 pN accumulated in one distal micron results in a force of $\tilde{F}_0^{(1)} \approx 300$ pN, compatible with $\tilde{\Omega}_0$ for *Chlamydomonas*. If $\sim$5% of this force

results in a torque over a distance of 0.015 μm, we obtain $M \approx 0.25$ pN μm, used for *Chlamydomonas*. For bull sperm, with a smaller $\tilde{\Omega}_0$, we used $M \approx 0.025$ pN μm instead.

The stiffnesses were calculated as follows: a doublet has 24 protofilaments compared to 13 in a microtubule. The bending stiffness scales as area squared, and so $\kappa_{\text{db}} \approx (24/13)^2\kappa_{\text{mt}} \approx 80$ pN μm^2, with $\kappa_{\text{mt}} \approx 23$ pN μm^2 for microtubules [41]. This results in $\kappa_1 \approx 115$ pN μm^2 and $\bar{\kappa} = 9\kappa_{\text{db}} \approx 700$ pN μm^2, comparable to measurements of sea urchin sperm [42]. The sliding stiffness k_s was determined in Ref. [43], and it corresponds to d between 3.5 and 10 μm; we chose $d \approx 6$ μm. The resulting distal twist angle for bull sperm is 0.04 rad, while for *Chlamydomonas* it is 0.25 rad.

The friction coefficients are $\xi_\parallel \approx 2\pi\eta/\ln(2h/a_0)$ and $\xi_\perp \approx 2\xi_\parallel$, where η is the viscosity of the surrounding fluid [7,42] and $h \approx 4$ μm the distance between the axoneme and the surface. For water at 22 °C we have $\eta = 0.96\,10^{-3}$ pN s μm^{-2}, which for $L \approx 10$ μm results in $\xi_\parallel \approx 0.0017$ pN s μm^{-2}. For the head of bull sperm, we use $\xi_{\text{trans}} = 6\pi r\alpha_t\eta$ and $\xi_{\text{rot}} = 8\pi\alpha_r r^3\eta$ [42], where r is the radius of the head and $\alpha_t = 1/(1 - 9/16)$ and $\alpha_r = 1/(1 - 1/8)$ are corrections due to the proximity to a wall [44]. In Ref. [7] it was observed that sliding controlled beating patterns require a large head friction. We take $r \approx 10$ μm, large for bull sperm but adequate for other species [45]. This results in $\xi_{\text{rot}} \approx 35$ pN s μm and $\xi_{\text{trans}} = 0.45$ pN s μm^{-1}. The values of the response coefficients for *Chlamydomonas* wild-type beats were $\zeta = -i221$ μm and $\chi = -1645$ pN/μm^2, for the *mbo2* mutant $\zeta = -i235$ μm and $\chi = -1916$ pN/μm^2, and for bull sperm $\chi = (-5516 - i10138)$ pN/μm^2.

The torsional stiffness of the axoneme could have contributions from the torsional stiffness κ_3 of individual microtubule doublets, which for simplicity we have not included in our discussion. This contribution becomes relevant when doublets are constrained not to rotate around their axis, and results in a net torsional stiffness $\kappa_3 + a_0^4 k_s$. Estimating $\kappa_3 \sim \kappa_1$, we have that $\kappa_3/(a_0^4 k_s) \sim (d/a_0)^2 \sim 10^3$. In this case, the torque necessary to twist the axoneme would be larger, and the twist would decay faster along the axonemal length.

[1] D. Nicastro, C. Schwartz, J. Pierson, R. Gaudette, M. E. Porter, and J. Richard McIntosh, The molecular architecture of axonemes revealed by cryoelectron tomography, Science **313**, 944 (2006).

[2] G. Pigino and T. Ishikawa, Axonemal radial spokes: 3d structure, function and assembly, Bioarchitecture **2**, 50 (2012).

[3] C. J. Brokaw, Direct measurements of sliding between outer doublet microtubules in swimming sperm flagella, Science **243**, 1593 (1989).

[4] P. Satir and T. Matsuoka, Splitting the ciliary axoneme: Implications for a "switch-point" model of dynein arm activity in ciliary motion, Cell Motil. Cytoskeleton **14**, 345 (1989).

[5] C. J. Brokaw, Thinking about flagellar oscillation, Cell Motil. Cytoskeleton **66**, 425 (2009).

[6] C. J. Brokaw, Molecular mechanism for oscillation in flagella and muscle, Proc. Natl. Acad. Sci. (USA) **72**, 3102 (1975).

[7] I. H. Riedel-Kruse, A. Hilfinger, J. Howard, and F. Jülicher, How molecular motors shape the flagellar beat, HFSP J. **1**, 192 (2007).

[8] S. Camalet and F. Jülicher, Generic aspects of axonemal beating, New J. Phys. **2**, 24 (2000).

[9] F. Jülicher and J. Prost, Spontaneous Oscillations of Collective Molecular Motors, Phys. Rev. Lett. **78**, 4510 (1997).

[10] C. J. Brokaw, Computer simulation of flagellar movement ix. oscillation and symmetry breaking in a model for short flagella and nodal cilia, Cell Motil. Cytoskeleton **60**, 35 (2005).

[11] C. J. Brokaw, Bend propagation by a sliding filament model for flagella, J. Exp. Biol. **55**, 289 (1971).

[12] K. E. Machin, Wave propagation along flagella, J. Exp. Biol. **35**, 796 (1958).

[13] P. Sartori, V. F. Geyer, A. Scholich, F. Jülicher, and J. Howard, Dynamic curvature regulation accounts for the

symmetric and asymmetric beats of chlamydomonas flagella, eLife **5**, e13258 (2016).

[14] V. F. Geyer, P. Sartori, B. M. Friedrich, F. Jülicher, and J. Howard, Independent control of the static and dynamic components of the chlamydomonas flagellar beat, Curr. Biol. **26**, 1098 (2016).

[15] N. D. Derr, B. S. Goodman, R. Jungmann, A. E. Leschziner, W. M. Shih, and S. L. Reck-Peterson, Tug-of-war in motor protein ensembles revealed with a programmable dna origami scaffold, Science **338**, 662 (2012).

[16] A. P. Carter, J. E. Garbarino, E. M. Wilson-Kubalek, W. E. Shipley, C. Cho, R. A. Milligan, R. D. Vale, and I. R. Gibbons, Structure and functional role of dynein's microtubule-binding domain, Science **322**, 1691 (2008).

[17] C. B. Lindemann, A model of flagellar and ciliary functioning which uses the forces transverse to the axoneme as the regulator of dynein activation, Cell Motil. Cytoskeleton **29**, 141 (1994).

[18] P. V. Bayly and K. S. Wilson, Equations of interdoublet separation during flagella motion reveal mechanisms of wave propagation and instability, Biophys. J. **107**, 1756 (2014).

[19] S. Yamaguchi, K. Saito, M. Sutoh, T. Nishizaka, Y. Y. Toyoshima, and J. Yajima, Torque generation by axonemal outer-arm dynein, Biophys. J. **108**, 872 (2015).

[20] R. D. Vale and Y. Yano Toyoshima, Rotation and translocation of microtubules in vitro induced by dyneins from tetrahymena cilia, Cell **52**, 459 (1988).

[21] T.-W. Su, L. Xue, and A. Ozcan, High-throughput lensfree 3d tracking of human sperms reveals rare statistics of helical trajectories, Proc. Natl. Acad. Sci. (USA) **109**, 16018 (2012).

[22] J. F. Jikeli, L. Alvarez, B. M. Friedrich, L. G. Wilson, R. Pascal, R. Colin, M. Pichlo, A. Rennhack, C. Brenker, and U. Benjamin Kaupp, Sperm navigation along helical paths in 3d chemoattractant landscapes, Nat. Commun. **6**, 7985 (2015).

[23] M. Hines and J. J. Blum, On the contribution of dynein-like activity to twisting in a three-dimensional sliding filament model, Biophys. J. **47**, 705 (1985).

[24] A. Hilfinger and F. Jülicher, The chirality of ciliary beats, Phys. Biol. **5**, 016003 (2008).

[25] C. Heussinger, F. Schüller, and E. Frey, Statics and dynamics of the wormlike bundle model, Phys. Rev. E **81**, 021904 (2010).

[26] R. Everaers, R. Bundschuh, and K. Kremer, Fluctuations and stiffness of double-stranded polymers: Railway-track model, Europhys. Lett. **29**, 263 (1995).

[27] G. G. Vernon and D. M. Woolley, Basal sliding and the mechanics of oscillation in a mammalian sperm flagellum, Biophys. J. **87**, 3934 (2004).

[28] V. Mukundan, P. Sartori, V. F. Geyer, F. Jülicher, and J. Howard, Motor regulation results in distal forces that bend partially disintegrated *chlamydomonas* axonemes into circular arcs, Biophys. J. **106**, 2434 (2014).

[29] G. I. Bell, Models for the specific adhesion of cells to cells, Science **200**, 618 (1978).

[30] B. M. Friedrich, I. H. Riedel-Kruse, J. Howard, and F. Jülicher, High-precision tracking of sperm swimming fine structure provides strong test of resistive force theory, J. Exp. Biol. **213**, 1226 (2010).

[31] T.-W. Su, I. Choi, J. Feng, K. Huang, E. McLeod, and A. Ozcan, Sperm trajectories form chiral ribbons, Sci. Rep. **3**, 1664 (2013).

[32] R. A. Segal, B. Huang, Z. Ramanis, and D. J. Luck, Mutant strains of chlamydomonas reinhardtii that move backwards only, J. Cell Biol. **98**, 2026 (1984).

[33] D. Eshel and C. J. Brokaw, New evidence for a "biased base-line" mechanism for calcium-regulated asymmetry of flagellar bending, Cell Motil. Cytoskeleton **7**, 160 (1987).

[34] J. Elgeti, U. Benjamin Kaupp, and G. Gompper, Hydrodynamics of sperm cells near surfaces, Biophys. J. **99**, 1018 (2010).

[35] M. Bessen, R. B. Fay, and G. B. Witman, Calcium control of waveform in isolated flagellar axonemes of chlamydomonas, J. Cell Biol. **86**, 446 (1980).

[36] K. E. Machin, The control and synchronization of flagellar movement, Proc. R. Soc. London, Ser. B **158**, 88 (1963).

[37] D. R. Brumley, K. Y. Wan, M. Polin, and R. E. Goldstein, Flagellar synchronization through direct hydrodynamic interactions, Elife **3**, e02750 (2014).

[38] J. Gray and G. J. Hancock, The propulsion of sea-urchin spermatozoa, J. Exp. Biol. **32**, 802 (1955).

[39] R. E. Johnson and C. J. Brokaw, Flagellar hydrodynamics. A comparison between resistive-force theory and slender-body theory, Biophys. J. **25**, 113 (1979).

[40] F. Perrin, Mouvement brownien d'un ellipsoide-i. dispersion diélectrique pour des molécules ellipsoidales, J. Phys. Radium **5**, 497 (1934).

[41] F. Gittes, B. Mickey, J. Nettleton, and J. Howard, Flexural rigidity of microtubules and actin filaments measured from thermal fluctuations in shape, J. Cell Biol. **120**, 923 (1993).

[42] J. Howard, *Mechanics of Motor Proteins and the Cytoskeleton* (Sinauer, Sunderland, MA, 2001).

[43] D. W. Pelle, C. J. Brokaw, K. A. Lesich, and C. B. Lindemann, Mechanical properties of the passive sea urchin sperm flagellum, Cell Motil. Cytoskeleton **66**, 721 (2009).

[44] J. Leach, H. Mushfique, S. Keen, R. Di Leonardo, G. Ruocco, J. M. Cooper, and M. J. Padgett, Comparison of faxén's correction for a microsphere translating or rotating near a surface, Phys. Rev. E **79**, 026301 (2009).

[45] J. M. Cummins and P. F. Woodall, On mammalian sperm dimensions, J. Reproduction Fertility **75**, 153 (1985).